Experimental and Theoretical Investigations of Porous Structure Formation in Electrospun Fibers

Pratyush Dayal,† Jing Liu,‡ Satish Kumar,‡ and Thein Kyu*,†

Department of Polymer Engineering, University of Akron, Akron, Ohio 44325-0301, and School of Polymer, Textile, and Fiber Engineering, Georgia Institute of Technology, Atlanta, Georgia 30332-0295

Received June 26, 2007; Revised Manuscript Received July 27, 2007

ABSTRACT: The development of internal microstructure in electrospun fibers has been investigated both experimentally and theoretically. Various morphologies such as tubes, beads, and porous structures have been observed experimentally during electrospinning from amorphous polymer solutions such as poly(methyl methacrylate)/methylene chloride and poly(styrene)/tetrahydrofuran. The dynamics of electrospinning is modeled based on multiple virtual strands of beads connected by Maxwell's elements in a cylindrical coordinate system. Concurrently, spatiotemporal growth of the porous structure is calculated in the framework of Cahn−Hilliard time-evolution equation under the quasi steady state assumption coupled with the solvent evaporation rate equation. The coarse-grain simulation reveals the real-time formation of pores along the spinline of the electrospun fiber as the concentration traverses across the phase diagram of the amorphous polymer solution.

Introduction

Electrospinning,[1,2] first conceptualized in the early 1930s,[3] has recently made significant progress in producing nanofibers,[4] continuous core/shell nanofibers,[5,6] as well as continuous hollow nanofibers[7] from polymer solutions[8] or melts.[9] The recent advances include fabrication of continuous metal,[10] ceramic,[11] and composite nanofibers.[12] Over 50 kinds of synthetic and natural polymer fibers have been produced using this technique with fiber diameters ranging from tens of nanometers to a few micrometers.[13] By virtue of a high surface area to mass ratio, nonwoven electrospun fiber mats have afforded potentially advantageous performance in the fields encompassing tissue engineering[14] to membrane science.[15] The large surface area created by electrospun fibers is important when considering end use applications, for instance, porous surface of a known size are required if nanoparticles need to be deposited on the fiber substrate or if drug molecules are to be incorporated for controlled release. Porous fibers are useful for chemical filtration or the preparation of functional nanotubes via fiber templates. One can take advantage of porous surface topologies of the fibers to control wetting properties and adsorption behavior. Thus, fundamental knowledge of the spinning dynamics in relation to the emerged internal structure such as shape, texture, and morphology of microfibers is indispensable. The link between electrospinning parameters and emerged fiber morphology will allow for the design of polymeric fibers to meet specific needs.

The morphology of the electrospun fibers is governed by several factors such as applied electrical voltage, flow rate, phase diagram, and solution properties of polymers including viscoelasticity, spinnability, temperature, competition between the rates of phase separation and solvent evaporation. When electrospinning of polymer solution is carried out from volatile solvents,[16−18] porous surface features are created predominantly.

In electrospinning, a polymer solution of desired concentration is placed in a pipet attached to a needle at its end and the piston is used to push the solution out of the needle. The polymer solution oozes out and forms a suspended droplet. When a high voltage is applied to the needle tip, the induced surface charges transform the suspended droplet to a conical shape, known as Taylor's cone, due to the electrostatic repulsion. When this electrostatic repulsion overcomes the surface tension, the fiber jet shoots out from the droplet and deposits on the grounded collector plate. By virtue of the imbalance of Coulombic force due to electrical charges, surface tension, and viscoelastic force, the fiber is displaced slightly in the transverse direction, thereby causing bending instability which in turns drives the fiber to wiggle.

Yarin and Reneker[19,20] were the first to model the dynamics of the electrospinning process. Their modeling of the dynamics of electrospinnning is based on the balance of the forces described above. The trajectory of the fiber is calculated in accordance with Newton's second law of motion, assuming the fiber jet to consist of a strand of charged beads which are connected together by Maxwell elements. While their model captures the wiggling dynamics of the jet, the single strand model cannot probe the development of internal microstructure.

In this paper, we extend the bead model developed by Yarin and Reneker[19,20] to multiple virtual strands of beads because of its capability in capturing the fiber wiggling (or whipping) dynamics. More importantly, their model takes into account the solvent evaporation, which plays a pivotal role in determining the internal fiber morphology of the electrified jet to be described here. The time taken by the fiber to reach the collector plate is of the order of milliseconds, and hence the in situ monitoring of the internal structure development is not feasible, at least experimentally. This is the source of motivation of the present theoretical modeling and simulation to describe the real-time evolution of microstructure in order to provide guidance to the actual electrospinning process.

Experimental Procedures

The polymers used in this work were purchased from Aldrich having reported molecular weight values of $\bar{M}_w = 300\,000$ g/mol for isotactic poly(methyl methacrylate) (*i*PMMA), and two atactic poly(methyl methacrylate) (*a*PMMA), having molecular weights

† Department of Polymer Engineering, University of Akron.
‡ School of Polymer, Textile, and Fiber Engineering, Georgia Institute of Technology.

10.1021/ma071418l CCC: $37.00
Published on Web 09/14/2007

of $\bar{M}_w = 350\,000$ and $\bar{M}_w = 996\,000$ g/mol, which will be hereafter referred to as lower and higher molecular weight *a*PMMA respectively in relative terms. Polystyrene (PS) having $\bar{M}_w = 100\,000$ g/mol was obtained from Dow Chemical Co. Solvents, such as methylene chloride (MC) and tetrahydrofuran (THF), were purchased from Aldrich and were used as received.

Electrospinning experiments were carried out at room temperature in a fume hood under the horizontal configuration at a relative humidity of 40%. A volumetric flow rate of 2 mL/h was applied to an 18-gauge stainless steel needle. The potential difference between the needle and the collector plate (grounded aluminum foil) was 22 kV at a distance of 100 mm.

The samples were gold coated and were characterized by scanning electron microscopy (SEM) using thermally assisted field emission gun (FEG) operated at 10 kV. The specific surface area of the porous fiber mat was measured by means of Brunauer−Emmett−Teller (BET) approach.

Theoretical Modeling. The electrospinning dynamics is described in terms of arrays of multiple strands consisting of charged beads arranged in a cylindrical coordinate system. These beads are connected to each other by Maxwell elements which consist of a spring having modulus, G and a dashpot having viscosity, η. Furthermore, each bead (i,j) is surrounded by four adjacent beads that are directed up (subscript u), down (subscript d), left (subscript l), and right (subscript r) of the bead (i,j); referring to $+z$, $-z$, $+\theta$ and $-\theta$ directions, respectively. The dynamics of electrojet is modeled based on the Newton's second law of motion that describes the force balance among Coulombic force due to electrical charges, surface tension, viscoelastic force, and applied electric field, in what follows[19,20]

$$\frac{d m\mathbf{v}_{ij}}{dt} = \sum_{\substack{i=1 \\ i,j\neq p,q}}^{M}\sum_{j=1}^{N} \frac{e^2}{R_{ij,pq}^{\,3}}(\mathbf{r}_{ij} - \mathbf{r}_{pq}) - e\frac{V_0}{h}\hat{\mathbf{k}} - \alpha\pi(a_{av})^2 k_{ij}[\mathrm{sign}(x_{ij})\hat{\mathbf{i}} + \mathrm{sign}(y_{ij})\hat{\mathbf{j}}] + \pi a_{uij}^{\,2}\frac{\sigma_{uij}}{l_{uij}}(\mathbf{r}_{i,j+1} - \mathbf{r}_{i,j}) - \pi a_{dij}^{\,2}\frac{\sigma_{dij}}{l_{dij}}(\mathbf{r}_{i,j} - \mathbf{r}_{i,j-1}) + \pi a_{rij}^{\,2}\frac{\sigma_{rij}}{l_{rij}}(\mathbf{r}_{i+1,j} - \mathbf{r}_{i,j}) - \pi a_{lij}^{\,2}\frac{\sigma_{lij}}{l_{lij}}(\mathbf{r}_{i,j} - \mathbf{r}_{i-1,j}) \quad (1)$$

where m is the mass of the bead which varies in time due to solvent evaporation. $\mathbf{v}$ is the velocity of the bead, $\mathbf{r}$ is the position vector, σ is the stress, e is the electrical charge on the bead, V_0 is the applied voltage, h is the distance between the spinneret and the collector plate, α is the surface tension coefficient, k is the curvature, and a is the diameter of the strain elements of length l. The relaxation time of the polymer is treated as a function of local polymer concentration[21] given by

$$\frac{\vartheta}{\vartheta_0} = \frac{c_p}{c_{p0}} \quad (2)$$

where ϑ_0 and c_{p0} are the initial values of relaxation time and polymer concentration, respectively. The polymer solution viscosity depends on the local polymer concentration according to[22]

$$\eta = 10^P \times 10^{Q(c_p)^q} \quad (3)$$

where the value of q ranges from $q = 0.1-1.0$ and $Q = 1$. By definition, the modulus of the spring in the Maxwell element is given by $G = \eta/\vartheta$. In the phase separating system, the concentrations of polymer-rich and solvent-rich regions are different locally and thus the local stress would vary in a manner dependent on the local modulus and viscosity. The temporal evolution of such local stress may be treated according to the standard Maxwell equation as follows

$$\frac{d\sigma}{dt} = \frac{c_{p0}}{c_p}\left[\left(\frac{\eta}{\eta_0}\right)\frac{G_0}{l}\frac{dl}{dt} - \frac{G_0}{\eta_0}\sigma\right] \quad (4)$$

where G_0 and η_0 are the initial values of modulus and viscosity, respectively. It is apparent that the above equation is governed by viscosity and polymer concentration ratios; therefore the value of exponent P of eq 3 is inconsequential.

To study the spatiotemporal development of fiber morphology during electrospinning it is essential to first establish the phase diagram of the polymer/solvent system to guide the trajectory of the concentration sweep across various coexistence regions of the phase diagram driven by solvent evaporation. This task may be implemented in the context of the Flory−Huggins free energy of mixing[23] which is given by

$$f_{local} = \frac{\phi_p}{n}\ln\phi_p + \phi_s \ln\phi_s + \chi\phi_p\phi_s \quad (5)$$

where n is the number of statistical segments, χ is the Flory−Huggins (FH) interaction parameter, ϕ_p and ϕ_s are the volume fractions of polymer and solvent, respectively. The FH interaction parameter is given as usual, i.e., $\chi = A + (\chi_c - A)T_c/T$, where A is athermal entropic contribution to the interaction parameter, T is absolute temperature, χ_c is the critical interaction parameter given by $\chi_c = 0.5(1 + 1/\sqrt{n})^2$ at a critical temperature, T_c. The equilibrium phase diagram was calculated self-consistently by equating the chemical potentials of each phase using the double tangent algorithm. In the phase diagram construction, the value of number of statistical segments was taken as $n = 55$ that approximately corresponds to $\bar{M}_w = 300\,000$ g/mol of PMMA.[24]

The dynamics of phase separation subjected to solvent evaporation can be modeled by inserting the FH free energy of isotropic mixing (given by eq 5) and the nonlocal interface gradient terms of de Gennes[25] into Cahn−Hilliard (CH) equation alternatively known as time-dependent Ginzburg Landau equation (TDGL model B).[26,27] The reaction-diffusion equation is expressed in terms of the CH equation coupled with the solvent loss, viz.

$$\frac{\partial c_s}{\partial t} = \nabla\cdot\left[\Lambda\angle\frac{\delta F}{\delta c_s} - k_m(c_s - c_s^{\,0})\hat{\mathbf{u}}_r\right] \quad (6)$$

where k_m is the mass transfer coefficient analogous to the solvent evaporation rate, c_s^0 is the solvent concentration far from the fiber interface and $\hat{u}_r$ is the unit vector in the radial direction. The total free energy of the system is defined as $F = \int_V (f_{local} + f_{nonlocal})\,dV$, where $f_{nonlocal} = \kappa|\nabla c_s|^2$ in which $\kappa = 1/36(a_p^2/c_p + a_s^2/c_s)$ is the interfacial gradient coefficient for concentration, a_p and a_s are characteristic lengths of polymer segment and solvent, respectively.[25] Λ represents the mobility that satisfies the Onsager reciprocity, i.e., $\Lambda = \Lambda_{0,pp}\Lambda_{0,ss}/(\Lambda_{0,pp} + \Lambda_{0,ss})$ and $\delta/\delta c_s$ signifies the functional derivative with respect to solvent concentration, c_s. The mobility of the constituent polymer and solvent can be related to the self-diffusion coefficients of polymer chain (D_p) and solvent molecule (D_s) according to $\Lambda_{0,pp} = nD_pc_p$ and $\Lambda_{0,ss} = D_sc_s$[28]. TDGL model B and electrospinning dynamic equations were solved in nondimensionless forms under the constraints of quasi steady-state approximation (QSSA),[29,30] which states that these two processes can be treated independently of each other provided that the elapsed time grid is infinitesimally small. Solving eqs 1, 4, and 6 iteratively in dimensionless form, the spatiotemporal evolution of domain morphology can be coupled to the electrospinning dynamics. The dimensionless length scale is $\bar{l} = l/L$, the dimensionless time is given by $\bar{t} = tG_0/\eta_0$, the dimensionless stress is taken as $\bar{\sigma} = \sigma/G_0$ and the dimensionless concentration is given by $\bar{c}_s = c_s/c_{s0}$, where c_{s0} is the initial solvent concentration. The force balance equation may be expressed in dimensionless form as

$$\frac{d\bar{\mathbf{v}}_{ij}}{d\bar{t}} = \frac{d^2\bar{\mathbf{r}}_{ij}}{d\bar{t}^2} = Q\sum_{\substack{i=1\\ i,j\neq p,q}}^{M}\sum_{j=1}^{N}\frac{1}{\bar{R}_{ij,pq}^{\ 3}}(\bar{\mathbf{r}}_{ij}-\bar{\mathbf{r}}_{pq}) - V\hat{\mathbf{k}} - S\frac{\gamma_{ij}}{\bar{l}_{av}}[\mathrm{sign}(\bar{x}_{ij})\hat{\mathbf{i}} + \mathrm{sign}(\bar{y}_{ij})\hat{\mathbf{j}}] + F_{ve}\left[\frac{\bar{\sigma}_{uij}}{\bar{l}_{uij}}(\bar{\mathbf{r}}_{i,j+1}-\bar{\mathbf{r}}_{i,j}) - \frac{\bar{\sigma}_{dij}}{\bar{l}_{dij}}(\bar{\mathbf{r}}_{i,j}-\bar{\mathbf{r}}_{i,j-1}) + \frac{\bar{\sigma}_{rij}}{\bar{l}_{rij}}(\bar{\mathbf{r}}_{i+1,j}-\bar{\mathbf{r}}_{i,j}) - \frac{\bar{\sigma}_{lij}}{\bar{l}_{lij}}(\bar{\mathbf{r}}_{i,j}-\bar{\mathbf{r}}_{i-1,j})\right] \quad (7)$$

along with the reaction diffusion equation given as

$$\frac{\partial\bar{c}_s}{\partial\bar{t}} = \bar{\nabla}\cdot\left[W\bar{c}^2\bar{\nabla}\left(\frac{\delta f_{local}}{\delta\bar{c}_s} - U\frac{\delta f_{nonlocal}}{\delta\bar{c}_s}\right) - K_m(\bar{c}_s - \bar{c}_s^{\,0})\hat{\mathbf{u}}_r\right] \quad (8)$$

where $1/\bar{l}_{av} = (1/\sqrt{\bar{l}_{uij}} + 1/\sqrt{\bar{l}_{dij}})^2$ and the over bar indicates the dimensionless operator. The relationships between the materials and the dimensionless parameters are given in Table 1.

Results and Discussion

In order to reduce the variables of the electrospinning process, all the experiments were carried out under a comparable condition for both PMMA/MC and PS/THF systems. Figure 1 shows morphology of electrospun *i*PMMA fibers, which has the BET surface area around 18 m^2/g. Inspection of the fiber cross-section, suggests that the pores are mostly located predominantly on the fiber surfaces. The porous *i*PMMA fiber has a larger surface area by virtue of the reduction in the fiber diameter. The pore size has a wide distribution from 30 nm to a few hundred nanometers in diameter which is governed by the competition between the phase separation dynamics and the fast evaporation rate of MC during the electrospinning process. These pores are deformed and oriented along the fiber axis, which may be attributed to shrinkage in fiber diameter while the fiber is elongated in the direction of stretching. The solvent-rich regions eventually transform into pores as solvent dries out. The pore structure formation seems to be fixed by vitrification as the glass transition temperature of the polymer solution increases with increasing polymer concentration due to solvent loss. From the SEM image of the fractured surface of the fiber, it can be inferred that the pores are present throughout the entire fiber.

The electron micrographs in Figure 2 demonstrate that microfibers spun from two different molecular weights ($\bar{M}_w \sim$ 350 000 and 996 000) of *a*PMMA/MC solutions were porous. The spinnability would be poor if the polymer solubility is poor or polymer concentration is low. If the solution viscosity is too low, electrospun fibers would be unstable and form beaded texture[31] or cups.[32] Despite the molecular weight difference of the two *a*PMMA samples, the bead-free porous fibers develop at the same concentration with comparable pore size and shape. In general, the viscosity of the polymer solution is known to be affected by molecular weight, and thus, one would need a higher polymer concentration to improve the spinnability. However, the lower molecular weight of *a*PMMA utilized here may be already sufficiently high (i.e., $\bar{M}_w \sim$ 350 000) such that the same concentration may be adequate to obtain the bead-free fiber.

Although the molecular weights of *i*PMMA and lower molecular weight *a*PMMA are comparably close; *i*PMMA produces bead-free fibers at around 4 wt %, whereas a higher concentration of 14 wt % was needed to produce bead-free fibers in the case of *a*PMMA ($\bar{M}_w \sim$ 350 000). This in turn suggests that the spinnability (or solution viscosity) could be affected by polymer tacticity. The formation of beaded fiber may be attributed to the instability of the fiber jet associated with the poor spinnability of the polymer solution which depends on polymer concentration, tacticity, and molecular weight.

In the case of PS/THF solution, a concentration of 29 wt % was needed to produce continuous (beadless) porous fibers with a diameter of around 5 μm with porous structures. According to the SEM images of Figure 3 and the surface area measured, the pores have an average diameter of approximately 30 nm. The PS fiber reveals highly porous textures. However, its surface area is only 2 m^2/g due to its larger fiber diameter, which is significantly smaller than that of the case of *i*PMMA, i.e., ~18 m^2/g. As pointed out earlier, the formation of porous fibers in electrospinning strongly depends on the solubility, viscosity, and concentration, among others.

The formation of porous fiber was first reported by Casper et al.[17] who demonstrated that electrospinning of PS/THF solution into the humid environment (i.e., 60% humidity) of can produce the porous structure. Recently, Srinivasarao et al.[33] reported the formation of a three-dimensionally ordered array of bubbles in a phase segregated thin PS film induced by the breath-moisture. In the present case, the porous fiber can be spun from a fast drying solvent such as MC or THF. It is well documented that the solvent quality can be easily reduced by the surrounding moisture, which in turn, could drive liquid−liquid-phase separation leading to the porous fiber formation.[34] One possible account is that both MC and THF are known to be water-soluble and thus would be sensitive to a minute level of moisture. The reduction in solvent quality due to such moisture absorption of the solvent will open up the upper critical solution temperature (UCST) gap which eventually would trigger the phase separation during electrospinning.

In general, four phase separation mechanisms can be envisaged to produce porous membranes: (i) thermally induced phase separation (TIPS), (ii) immersion precipitation, (iii) air-casting of the polymer solution, and (iv) precipitation from the vapor phase.[34] A detailed discussion of each type of phase separation in relation to pore formation has been reported by Megelski et al.,[18] concluding that thermodynamic instability is the driving force behind phase separation. Decreasing temperature, loss of solvent, or increase in nonsolvent (moisture) causes a solution

Table 1. Materials and Dimensionless Parameters Utilized in the Simulations

materials parameters		dimensionless parameters		
symbols	values	nomenclature	relationships	values
e^a	10^{-9} C	charge	$Q = e^2\eta_0^2/G_0^2mL^3$	1000
G_0	2.0 Pa	viscoelastic force	$F_{ve} = \pi a_0^2\eta_0^2/mG_0L$	0.10
η_0	2.0×10^{-2} Pa s	surface tension	$S = \alpha\pi a_0^2\eta_0^2/4mG_0^2L^2$	0.0
V_0	8 kV	voltage	$V = eV_0\eta_0/mG_0Lh$	40
h	10 mm	height	$H = h/L$	10^5
D_s^b	2.5×10^{-8} m^2/s	mobility	$W = \eta_0D_s/G_0L^2$	250
D_p^b	2.5×10^{-10} m^2/s			
a_p^c	10^{-7} m	interfacial gradient coeff	$U = a_p^2/L^2$	1.0

[a] Value taken from ref 19. [b] Value taken from ref 36. [c] Value taken from ref 37.

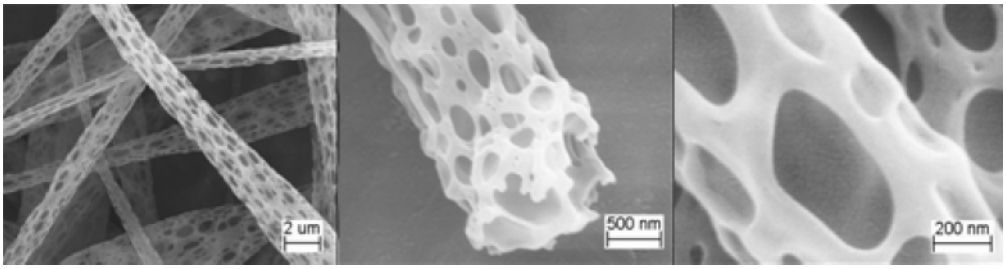

Figure 1. Porous fibers from solution of 2 wt % *i*PMMA in methylene chloride at different magnifications.

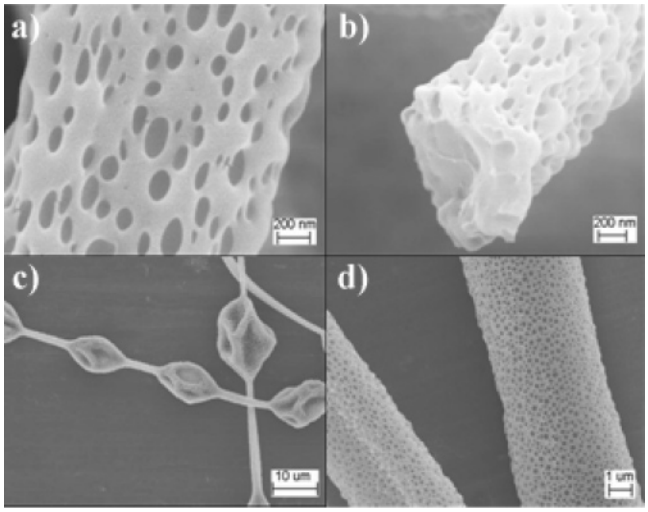

Figure 2. Porous fibers from *a*PMMA/MC from M_w of 350 000 g/mol (a) 10 wt % and (b) 12 wt % and from M_w of 996 000 g/mol (c) 10 wt % and (d) 12 wt %.

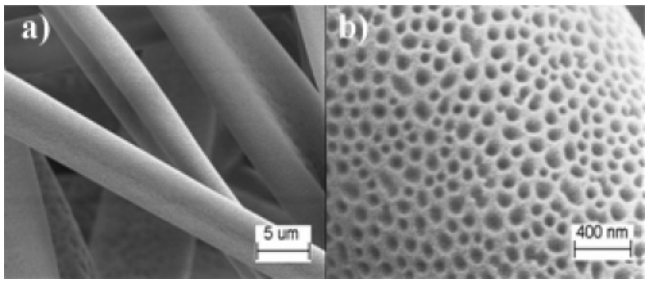

Figure 3. (a) Porous fibers from 29 wt % PS/THF. (b) Magnification surface feature of fibers from part a.

to become thermodynamically unstable during the electrospinning process, which in turn drives phase separation, leading to pore formation.

In an effort to elucidate the mechanism of porous fiber formation, a model simulation was performed for a polymer solution having an upper critical solution temperature (UCST) from the initial polymer volume fraction of 0.03 at the temperature of $T/T_c = 1.25$ and a flow rate of 9 mL/h. The values of material parameters used for this calculation are tabulated in Table 1. These parameters were converted to the corresponding dimensionless parameters (see Table 1) using the length scale $L = 0.1$ μm and time scale of $\vartheta_0 = 10$ ms. The diffusivities were taken to be proportional[35] to $T^{3/2}$, while the mass transfer coefficient or the solvent evaporation rate constant k_m is related to diffusivities by Sherwood number.[20] The solvent concentration, c_s^0 was taken as 0.01 for all cases that corresponds to 32% relative humidity at ambient temperature. The ratio a_p/a_s was taken as unity for simplicity. Subsequent calculations were performed utilizing the same dimensionless parameter values, unless stated otherwise. Such a phase diagram is shown in Figure 4a for the solution of *a*PMMA of molecular weight $\bar{M}_w = 300\,000$ g/mol in MC. The coexistence curve is skewed toward the solvent-rich side due to the vast disparity of the molecular weight of MC and *a*PMMA. The phase diagram is characterized by three distinct regions, viz., the stable one-phase region, the unstable two-phase region, and the metastable regions. Depending on the thermal quenching or slow cooling into unstable or metastable regions, liquid−liquid-phase separation is known to occur by spinodal decomposition (SD) or by nucleation and growth (NG). The point indicated by open circle in Figure 4a corresponds to the initial concentration of the polymer and the arrow indicates how the system traverses along the concentration axis with continued solvent evaporation. One can witness in Figure 4b that the system is, and continues to be, in the isotropic state throughout the calculation. As a result, the polymer concentration simply increases along the spinline without any indication of internal structure on the fiber and nonporous dry fiber is obtained. Such textureless fiber formation is consistent with our previous finding of the solid fiber subjected to solvent evaporation.[29,30] A similar phase separation can be seen in a system undergoing solvent evaporation, in which polymer concentration increases gradually which pushes the system to traverse across the phase diagram.

The snapshot of the porous fibers formed from electrospinning, with reference to the phase diagram, is depicted in Figure 5. The simulations was carried out at $T/T_c = 0.95$ by varying the value of interfacial gradient coefficient, U. The black color corresponds to solvent-rich regions and the white color represents the polymer-rich regions (Figure 5, parts b and c). Initially there is no phase separation in the fiber although the polymer concentration has already reached the metastable gap of the

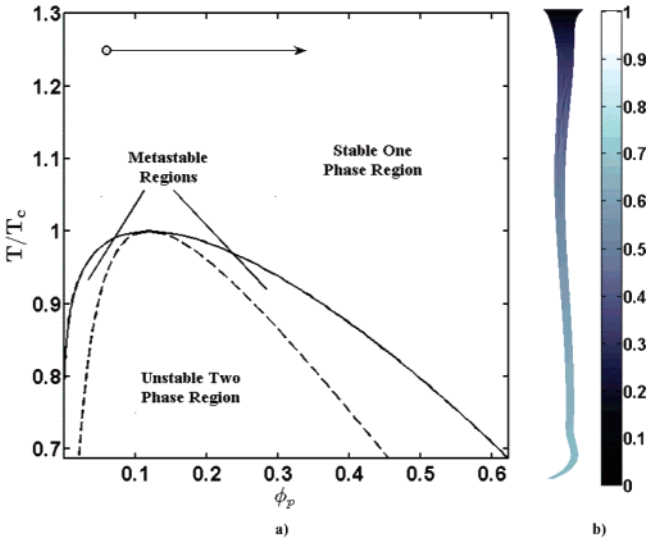

Figure 4. (a) Equilibrium phase diagram of *a*PMMA/MC system. The statistical segment length of *a*PMMA, $n = 55$ corresponds to $\bar{M}_w = 300\,000$ g/mol. (b) Single phase textureless fiber when electrospinning is carried out at the condition indicated in the phase diagram.

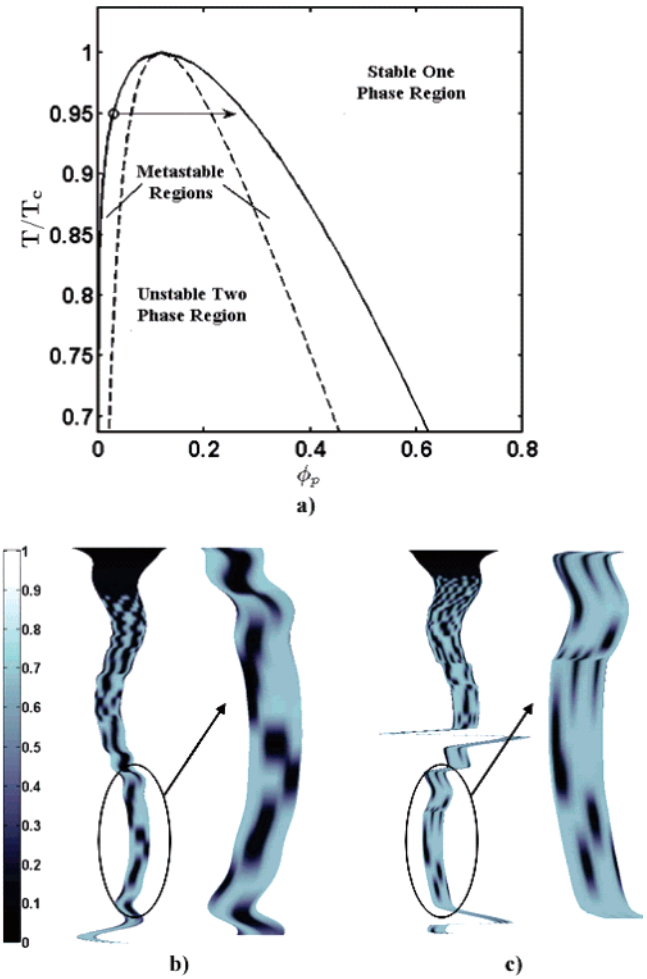

Figure 5. Effect of dimensionless interface gradient coefficient, U, on the pore sizes of the electrospun fibers: (a) spinning condition with reference to the phase diagram; (b) electrospun fiber at $U = 1.0$; (c) electrospun fiber at $U = 0.4$. The decrease in the value of interface gradient coefficient decreases the size of the pores.

UCST phase diagram which is probably due to the kinetic effect. The polymer concentration increases in the direction indicated by the arrow as a result of solvent evaporation and the system traverses across the phase diagram from the single phase region to the metastable region where polymer droplets can be discerned. With further increase of the polymer concentration, the droplet morphology transforms into an interconnected structure due to the domination by SD in the unstable region. This bicontinuous morphology further transforms into porous structure as the system enters the polymer-rich metastable region. It is seen that although the final structure of the fiber is porous, the aforementioned transformations of different morphologies can be captured along the spinline during the concentration sweep across the phase diagram. The value of interfacial gradient coefficient was decreased to $U = 0.4$ for the calculations in Figure 5c. It can be noticed from visual comparison between Figure 5, parts b and c, that decreasing the value of U reduces the pore size. That is to say decreasing the value of U (or κ) is equivalent to reducing penalty for formation of new surface, and thus formation of smaller solvent domains would be favorable.

Interfacial gradient coefficient U (or κ) is not the only variable that influences the pore size; solvent evaporation rate could affect the dynamics of pore formation. To examine the effect of solvent evaporation rate on pore formation, the simulations were carried out at several temperatures because changing

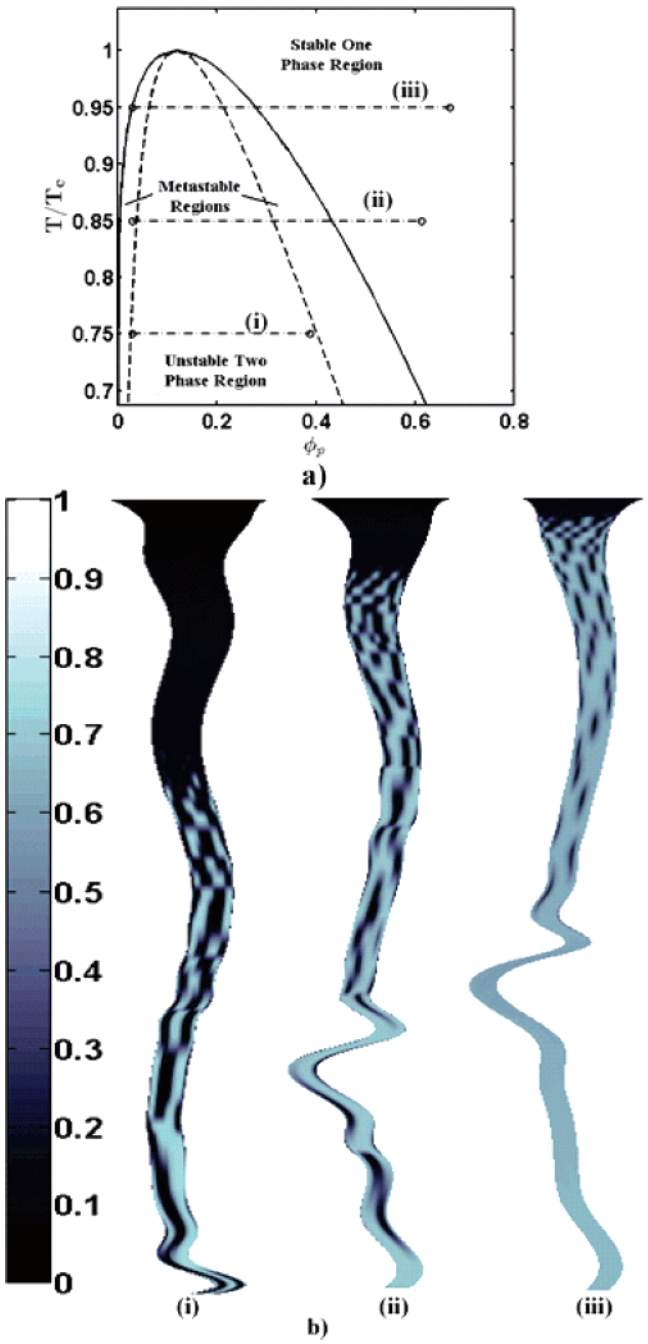

Figure 6. Simulated electrospun fiber from the spinneret (top) to the collector plate (bottom) with reference to the phase diagram (a) where (i), (ii) and (iii) represent the concentration sweeps at different temperatures. (b) Electrospun fiber in which dark regions represent solvent-rich regions and bright regions represent polymer rich regions. The pores are smaller in diameter as the temperature increases.

temperature automatically alters not only the phase separation rate, but also the solvent evaporation rate, and thus their interplay can be investigated. The value of applied voltage V was chosen to be 30. Figure 6 shows the influence of temperature of electrospinning on morphology development subject to the concentration sweep as the system passes through various coexistence regions of the UCST envelope. The horizontal dash-dot lines represent the trajectory of the concentration sweeps across the phase diagram at a given temperature, where the initial and final (i.e., at the collector plate) concentrations are indicated by open circles at the end of these lines. The corresponding fiber morphologies are displayed below the phase diagram. With increasing temperature from (i) to (iii), three notable features

are discerned in the electrospun fibers: (1) the single phase solvent-rich jet gets shorter, (2) the fiber diameter is reduced, and (3) the size of the phase-separated domains inside the fiber gets smaller. During the electrospinning at an elevated temperature shown in Figure 6b(iii), the solvent evaporation rate is very fast which in turn drives the polymer concentration to rise rapidly, thereby crossing the UCST phase diagram very quickly. The porous fiber morphology is developed in a shorter period that eventually exits to the single phase where a textureless solid fiber is formed. The growth step of polymer droplets in the metastable region and interconnectivity in the unstable spinodal region is probably missed due to the fast solvent evaporation rate. The formation of the polymer droplets and its subsequent transformation to the interconnected structure can be seen readily when the solvent evaporation is slowed down by reducing the spinning temperature (Figure 6b(i−ii)). However, the phase separation domains are larger than that in the fast solvent evaporation case shown in Figure 6b(iii). By virtue of the rapid rise in polymer concentration, not only does the fiber length get stretched out and the diameter get shrunk, but also it causes the solvent pockets (or cavities) to deform into the elongated shape.

It should be pointed out that the observed smaller phase separated domains within the microfiber at the high-temperature spinning is counterintuitive. In the case of conventional thermal quenching, the average domain size is expected to be larger at elevated temperature because the length scale is universally known to be inversely proportional to the supercooling. At higher temperatures, the solvent evaporation rate is expedited so much so that there is no sufficient time for the phase separated domains to ripen fully, therefore the domains may cease to grow and thus the average size may be smaller as compared to the low-temperature spinning case where the solvent evaporation is relatively slow. As can be expected, the enhanced solvent evaporation rate with increasing temperature makes the initial single phase morphology to become progressively shorter as demonstrated in Figure 5b(i−iii).

Except for the spinning at the highest temperature of Figure 6b(iii), the two-phase morphology persists in the single phase region of the phase diagram despite the fact that the system has already exited the UCST envelope. This finding may be attributed to the kinetic effect as the fiber touches the collector plate, the structure gets fixed due to solidification or vitrification. The vitrification effect (e.g., the increasing glass transition temperature of the polymer solution due to solvent loss) could prevent the structure from dissolving away (see a change from (i) to (ii)) even though the final polymer concentration may have already reached the single-phase region.

Conclusions

Porous fiber formation during electrospinning has been demonstrated experimentally as well as theoretically. The porous fibers are favored to form if the polymer/solvent system is partially miscible showing a UCST envelope at the electrospinning temperature, especially if the solvent utilized were volatile and sensitive to moisture absorption. The pore size depends on various factors such as surface energy and the solvent evaporation rates. The theoretical modeling illustrates the dynamics of pore formation demonstrating how the coupling between the microfiber morphology development and the electrospinning dynamics captures the morphology transition along the spinline driven by the concentration sweep across the UCST phase diagram.

Acknowledgment. The UA group expresses their gratitude to National Science Foundation, (Grants DMR 0209272 and DMR 0514942), the Ohio Board of Regents (Research Challenge Grant), and National Aeronautics and Space Administration, (Grant NCC-1-02002) for their support.

References and Notes

(1) Dzenis, Y. *Science* **2004**, *304*, 1917−1919.
(2) Li, D.; Xia, Y. N. *Adv. Mater.* **2004**, *16*, 1151−1170.
(3) Formhals, A. *United States Patent* **1934**, *1*, 504.
(4) Li, D.; Ouyang, G.; McCann, J. T.; Xia, Y. N. *Nano Lett.* **2005**, *5*, 913−916.
(5) Liu, J.; Wang, T.; Uchida, T.; Kumar, S. *J. Appl. Polym. Sci.* **2005**, *96*, 1992−1995.
(6) McCann, J. T.; Li, D.; Xia, Y. N. *J. Mater. Chem.* **2005**, *15*, 735−738.
(7) Li, D.; Xia, Y. N. *Nano Lett.* **2004**, *4*, 933−938.
(8) Mathew, G.; Hong, J. P.; Rhee, J. M.; Lee, H. S.; Nah, C. *Polym. Test.* **2005**, *24*, 712−717.
(9) Lyons, J.; Li, C.; Ko, F. *Polymer* **2004**, *45*, 7597−7603.
(10) Yu, N.; Shao, C. L.; Liu, Y. C.; Guan, H. Y.; Yang, X. H. *J. Colloid Interface Sci.* **2005**, *285*, 163−166.
(11) Li, D.; Herricks, T.; Xia, Y. N. *Appl. Phys. Lett.* **2003**, *83*, 4586−4588.
(12) Kedem, S.; Schmidt, J.; Paz, Y.; Cohen, Y. *Langmuir* **2005**, *21*, 5600−5604.
(13) Li, L.; Hsieh, Y. L. *Polymer* **2005**, *46*, 5133−5139.
(14) Zong, X. H.; Bien, H.; Chung, C. Y.; Yin, L. H.; Fang, D. F.; Hsiao, B. S.; Chu, B.; Entcheva, E. *Biomaterials* **2005**, *26*, 5330−5338.
(15) Nair, L. S.; Bhattacharyya, S.; Laurencin, C. T. *Expert Opin. Biol. Ther.* **2004**, *4*, 659−668.
(16) Bognitzki, M.; Czado, W.; Frese, T.; Schaper, A.; Hellwig, M.; Steinhart, M.; Greiner, A.; Wendorff, J. H. *Adv. Mater.* **2001**, *13*, 70.
(17) Casper, C. L.; Stephens, J. S.; Tassi, N. G.; Chase, D. B.; Rabolt, J. F. *Macromolecules* **2004**, *37*, 573−578.
(18) Megelski, S.; Stephens, J. S.; Chase, D. B.; Rabolt, J. F. *Macromolecules* **2002**, *35*, 8456−8466.
(19) Reneker, D. H.; Yarin, A. L.; Fong, H.; Koombhongse, S. *J. Appl. Phys.* **2000**, *87*, 4531−4547.
(20) Yarin, A. L.; Koombhongse, S.; Reneker, D. H. *J. Appl. Phys.* **2001**, *89*, 3018−3026.
(21) Yarin, A. L. *Free Liquid Jets and Films: Hydrodynamics and Rheology*; Longman, Harlow and Wiley: New York, 1993.
(22) Ziabicki, A. *Fundamentals of Fiber Formation*; Wiley: London, 1976.
(23) Flory, P. J. *Principles of Polymer Chemistry*; Cornell University Press: Ithaca, NY, 1953.
(24) Kyu, T.; Shen, C.; Chiu, H.-W. *Mol. Cryst. Liq. Cryst.* **1996**, *287*, 27−34.
(25) deGennes, P. G. *J. Chem. Phys.* **1980**, *72*, 4756−4763.
(26) Cahn, J. W.; Hilliard, I. E. *J. Chem. Phys.* **1958**, *28*, 258−267.
(27) Cahn, J. W. *Acta Mel.* **1961**, *9*, 795−801.
(28) Gunton, J. D.; Miguel, M. S.; Sahni, P. S. In *Phase Transitions and Critical Phenomena*; Domb, C., Lebowitz, J. L., Eds.; Academic Press: New York, 1983; Vol. 8, p 267.
(29) Guenthner, A. J.; Khombhongse, S.; Liu, W.; Dayal, P.; Reneker, D. H.; Kyu, T. *Macromol. Theory Simul.* **2006**, *15*, 87−93.
(30) Dayal, P.; Kyu, T. *J. Appl. Phys.* **2006**, *100*, 043512/1−6.
(31) Reneker, D. H.; Fong, H.; Chun, I. *Polymer* **1999**, *40*, 4585−4592.
(32) Liu, J.; Kumar, S. *Polymer* **2005**, *46*, 3211−3214.
(33) Srinivasarao, M.; Collings, D.; Philips, A.; Patel, S. *Science* **2001**, *292*, 79−83.
(34) Matsuyama, H.; Teramoto, M.; Nakatani, R.; Maki, T. *J. Appl. Polym. Sci.* **1999**, *74*, 159−170.
(35) Bird, R. B.; Stewart, W. E.; Lightfoot, E. N. *Transport phenomena*; John Wiley and Sons: New York, 1960.
(36) *Perry's Chemical Engineers' Handbook*, 7th ed.; Perry, R. H., Green, D. W., Eds.; McGraw-Hill: New York, 1997.
(37) *Polymer handbook*, 4th ed.; Brandrup, J., Immergut, J. E. H., Eds.; Wiley: New York, 1999.

MA071418L